

Article

Optimized Cooperative Control of Error Port-Controlled Hamiltonian and Adaptive Backstepping Sliding Mode for a Multi-Joint Industrial Robot

Xiaoyu Yang ^{1,2}  and Haisheng Yu ^{1,2,*}¹ College of Automation, Qingdao University, Qingdao 266071, China² Shandong Province Key Laboratory of Industrial Control Technology, Qingdao 266071, China

* Correspondence: yhsh_qd@qdu.edu.cn

Abstract: Robot joints driven by permanent magnet synchronous motors (PMSM) often cannot have both superior accuracy and rapidity when they track target signals. The robot joints have fine dynamic characteristics and poor steady-state characteristics when the signal controller is used, or they have fine steady-state characteristics and poor dynamic characteristics when the energy controller is used. It is hard to make robot joints that have both superior dynamic and steady-state characteristics at once using a single control method. In order to solve this problem, the strategy of optimized cooperative control is proposed. First, an error port-controlled Hamiltonian (EPCH) energy controller and an adaptive backstepping sliding mode (ABSM) signal controller are designed. Second, an optimized cooperative control coefficient based on the position error of a robot joint is designed; this enables the system to switch smoothly between the EPCH energy controller and ABSM signal controller. Next, the strategy of optimized cooperative control is designed. In this way, robot systems can combine the advantages of the EPCH energy controller and the ABSM signal controller. Finally, simulation results demonstrate that using the strategy of optimized cooperative control gives robot joints outstanding control performance in terms of tracking accuracy and response rapidity.

Keywords: robot joints; permanent magnet synchronous motors (PMSM); optimized cooperative control; error port-controlled Hamiltonian (EPCH); adaptive backstepping sliding mode (ABSM); optimized cooperative control coefficient

MSC: 70E60

Citation: Yang, X.; Yu, H. Optimized Cooperative Control of Error Port-Controlled Hamiltonian and Adaptive Backstepping Sliding Mode for a Multi-Joint Industrial Robot.

Mathematics **2023**, *11*, 1542. <https://doi.org/10.3390/math11061542>

Academic Editors: Mihail Ioan Abrudean and Vlad Muresan

Received: 24 February 2023

Revised: 17 March 2023

Accepted: 19 March 2023

Published: 22 March 2023



Copyright: © 2023 by the authors. Licensee MDPI, Basel, Switzerland. This article is an open access article distributed under the terms and conditions of the Creative Commons Attribution (CC BY) license (<https://creativecommons.org/licenses/by/4.0/>).

1. Introduction

In recent years, multi-degree-of-freedom (DOF) industrial robots have been widely used in assembly, handling and other industries [1–3]. They can replace repetitive machine-type manipulation, and they are servo devices that rely on their own power and control to achieve multiple functions. With the rapid development of modern manufacturing, requirements for the control accuracy, running speed and system stability of industrial robots are increasing [4].

A robot system includes a driving device, a transmission device and the robot body. Driving devices mostly adopt PMSM [5], due to PMSM having the characteristics of high accuracy, wide speed range, low speed and fast dynamic response. Transmission devices widely adopt harmonic drive. PMSM converts electromagnetic torque into joint torque using harmonic drive, which can drive the robot joints to complete specified motions and functions.

The transmission mechanism in harmonic drive is rolling transmission, and friction is represented by rolling friction. As a dynamic friction model, the LuGre friction model explains the relationship between nonlinear force, Coulomb friction, viscous friction and the Stribeck effect. It describes friction force as a function of relative velocity between the

contact surfaces [6–8]. The harmonic drive is divided into the motor side and the joint side in this paper. Dynamic equations based on the LuGre friction model are established in order to improve the generalized mathematical model of the robot joint servo system.

The process of researching PMSM-driven robot joints is currently accelerating, and researchers have made great progress in this area of science and technology innovation. However, there are still many problems to be solved related to the servo control of robot joint systems. In the actual industrial production, creating robot joints that have both superior response speed and control accuracy, and remain stable during the whole process of operation, has become a key technology problem in the research field of PMSM-driven robot joint servo control system [9,10].

Domestic and foreign researchers have carried out a large amount of research work with the aim of improving performance of control and optimization of PMSM-driven robot joints. Depending on the controller used, the design of servo control of robot joints can be divided into two types: signal control and energy control. From the point of view of signal control [11,12], the servo control system of a robot joint is considered to be a signal conversion device that converts the input position signal into the output position signal. Although a signal controller can achieve the control requirement of fast dynamic response, the electrical characteristics of PMSM and the friction characteristics of robot joints are not considered. Due to high energy consumption and loss of friction, the optimization of energy loss in the steady state cannot be achieved. Therefore, the steady-state error of the system is large, and vibration occurs during the operation of a robot joint when the signal controller is used alone. In contrast, from the point of view of energy control [13,14], the servo control system of a robot joint is considered an energy conversion device. It converts the given input energy into the actual output energy. The energy controller can cause the system to track accurately in the steady state and stabilise the joint during operation, but the dynamic response speed is very slow.

Based on the view of signal control, many control strategies have been proposed. These include backstepping control [15], sliding mode control [16], fuzzy control [17], robust control [18,19], adaptive control [20], etc.

The backstepping control (BC) algorithm is simple and makes the design process of a controller systematized and structured. BC is often combined with intelligent methods and other nonlinear methods in the position control of robot joint servo systems [21,22].

Sliding mode control (SMC) is extensively applied in nonlinear systems, due to its strong robustness against external disturbances and parameter perturbations. Traditional SMC has many obstacles in practical application; for instance, it cannot make systems converge in a limited time, and shows a obvious chattering phenomenon during the operation of the robot joints [23,24]. However, SMC has the merit of quick regulation, which can result in nonlinear systems having faster dynamic response speeds than with other control methods [25].

An accurate mathematical model cannot be established for the robot joint servo system, so fuzzy control [26] has been proposed. However, the steady-state error of the systems in this case is large and the control effect is unsatisfactory.

As a kind of robust control, H_∞ shows strong robustness in the field of controlling robot joints. In [27], a controller for robot joints is designed using a H_∞ frame. It can precisely follow target signals and has good robustness. However, the design scheme of H_∞ is complicated and difficult to implement. The above research algorithms all stem from the viewpoint of signal control. Although they promote the response speed of robot joint servo systems, their steady-state error rates are large.

At present, scientific researchers are concerned with research into algorithms approaching the problem from the viewpoint of energy control. Ortega et al. proposed the port-controlled Hamiltonian (PCH) [28–31] control method, which uses a dissipative PCH model to represent the dynamic system. It can diminish the steady-state error of a robot joint's servo system during operation. Nevertheless, the rapidity of this system is poor, and its dynamic properties are difficult to guarantee.

To sum up, both single signal control methods and energy control methods have their own weaknesses. In order to develop a system with both superior rapidity and accuracy at the same time, the strategy of optimized cooperative control is put forward in this paper. The strategy of optimized cooperative control adopts a optimized cooperative control coefficient based on the position error of robot joints, so that the system can smoothly switch between the signal controller and the energy controller. The signal controller occupies centre stage and guarantees the rapidity of system when the error of a joint is large. When the error is small, control switches from the signal controller to the energy controller. At this time, the energy controller occupies centre stage and guarantees the accuracy of the system. In this way, the robot joint benefits from the advantages of the signal controller and the energy controller. The system has short response time and low tracking error when robot joints are tracking target signals. Generalized mathematical models of the robot joint servo system are expressed by combining the robot body's dynamics equation, motor characteristics and joint friction. The EPCH energy controller and ABSM signal controller are both designed using the generalized mathematical model. A Gaussian function is used as the optimized cooperative control coefficient, and the strategy of cooperative optimization control of EPCH and ABSM is designed. Finally, simulation results show that this strategy results in a robot system that has both fast response speed and high tracking accuracy.

The structure of this article is as follows. In Section 2, the kinetic equation of a multi-joint industrial robot is given. In Section 3, the EPCH energy controller, ABSM signal controller and the strategy of optimized cooperative control are designed. In Section 4, we testify to the availability of optimized cooperative control through simulation results. The conclusion is given in Section 5.

2. Mathematical Model of Multi-Joint Industrial Robot

This paper takes the servo system of a 2-DOF robot as the object of study. The multi-joint industrial robot servo system is displayed in Figure 1. It includes three parts: PMSM, harmonic drive and robot body. The Lagrange's equation of the robot body is described as [32]

$$M(q)\ddot{q} + C(q, \dot{q})\dot{q} + G(q) = \tau_L - R_f\dot{q} - J^T F \quad (1)$$

where $q \in \mathbb{R}^2$, $\dot{q} \in \mathbb{R}^2$ and $\ddot{q} \in \mathbb{R}^2$ denote the position, velocity and acceleration, respectively. $M(q) \in \mathbb{R}^2$ is the positive and definite inertia matrix. $C(q, \dot{q}) \in \mathbb{R}^2$ includes the Coriolis and centripetal forces. $G(q) \in \mathbb{R}^2$ is the vector of gravity terms. $\tau_L \in \mathbb{R}^2$ is the moment of the robot joint. $R_f \in \mathbb{R}^2$ denotes the Coulomb friction coefficient matrix of robot joints. $F \in \mathbb{R}^2$ is a vector of external force. $J \in \mathbb{R}^2$ is the Jacobian matrix.

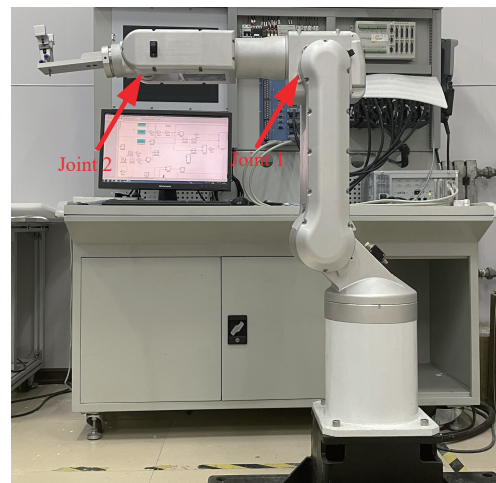


Figure 1. The multi-joint industrial robot servo system.

The parameters of robot body is presented in the Appendix A.

To establish the mathematical model of PMSM, the following conditions are described:

1. The influence of the core saturation phenomenon is not considered.
2. The damping effects of the permanent magnet and rotor are ignored.
3. The material of the permanent magnet is considered to be insulated.
4. It is determined that the magnetic circuit is linear and satisfies the superposition theorem.

In a synchronously rotating d - q reference frame, the model of the i -th ($i = 1, 2$) PMSM with implicit pole type ($L_{di} = L_{qi}$) can be described as [33]

$$\begin{cases} L_{di} \frac{di_{di}}{dt} = -R_{si}i_{di} + n_{pi}\omega_i L_{qi}i_{qi} + u_{di} \\ L_{qi} \frac{di_{qi}}{dt} = -R_{si}i_{qi} - n_{pi}\omega_i L_{di}i_{di} - n_{pi}\omega_i \Phi_i + u_{qi} \\ J_{mi} \frac{d\omega_i}{dt} = \tau_i - \tau_{Li} - R_{mi}\omega_i \\ \frac{d\theta_i}{dt} = \omega_i \end{cases} \quad (2)$$

$$\tau_i = \frac{3}{2}n_{pi} [(L_{di} - L_{qi})i_{di}i_{qi} + \Phi_i i_{qi}] \quad (3)$$

where τ_i is the electromagnetic torque of PMSM. τ_{Li} is the torque of the robot joint. u_{di} and u_{qi} denote the stator voltages of the d -axis and q -axis, respectively. L_{di} and L_{qi} denote the stator inductances of the d -axis and q -axis, respectively. i_{di} and i_{qi} denote the stator currents of the d -axis and q -axis, respectively. R_{si} is the stator resistance per phase. Φ_i is the rotor flux linking of the stator. n_{pi} is the number of pole pairs in PMSM. θ_i is the angle. J_{mi} is the moment of inertia in PMSM. R_{mi} is the friction coefficient of PMSM. ω_i is the angular velocity.

We can learn from $i_{di}^* = 0$ and $L_{di} = L_{qi}$ that

$$i_{qi}^* = \frac{2\tau_i}{3n_{pi}\Phi_i} \quad (4)$$

The i -th harmonic drive is decomposed into a dynamic model consisting of the motor side and joint side. The motor side is connected to the PMSM, and the joint side is connected to the robot joint.

The model of the motor side is

$$\tau_i = J_{gi}\ddot{\theta}_i + \tau_{gi} + \tau_{ci} \quad (5)$$

The model of the joint side is

$$\eta_i^{-1}\tau_{ci} = J_{di}\ddot{q}_i + \tau_{di} + \tau_{Li} \quad (6)$$

where τ_{ci} is the load moment of the motor side. τ_{gi} is the friction torque of the motor side. τ_{di} is the friction torque of the joint side. J_{gi} is the moment of inertia of the motor side. J_{di} is the moment of inertia of the joint side. $\ddot{\theta}_i$ is the angular acceleration of the motor shaft. \ddot{q}_i is the angular acceleration of the robot joint. η_i is the reduction ratio of the harmonic drive, and $\dot{q}_i = \eta_i \cdot \dot{\theta}_i$.

The LuGre model expression of τ_{gi} is

$$\begin{cases} \tau_{gi} = \sigma_{01i}z_{1i} + \sigma_{11i}\dot{z}_{1i} + \sigma_{21i}\omega_i \\ g_1(\omega_i) = F_{c1i} + (F_{s1i} - F_{c1i})e^{-\frac{\omega_i^2}{\omega_{s1i}^2}} \\ \dot{z}_{1i} = \omega_i - \frac{|\omega_i|}{g_1(\omega_i)}z_{1i} \end{cases} \quad (7)$$

where z_{1i} and \dot{z}_{1i} denote the average bristle deformation amount and deformation rate of the high-speed axis, respectively. F_{c1i} , F_{s1i} , ω_{s1i} , $g_1(\omega_i)$, respectively, denote the Coulomb friction, Stribeck friction, Stribeck velocity and static friction functions of high-speed shafts. σ_{01i} , σ_{11i} and σ_{21i} denote the bristle stiffness, bristle damping and viscous friction of the motor side, respectively.

The LuGre model expression of τ_{di} is

$$\begin{cases} \tau_{di} = \sigma_{02i}z_{2i} + \sigma_{12i}\dot{z}_{2i} + \sigma_{22i}\dot{q}_i \\ g_2(\dot{q}_i) = F_{c2i} + (F_{s2i} - F_{c2i})e^{-\frac{\dot{q}_i^2}{\omega_{s2i}^2}} \\ \dot{z}_{2i} = \dot{q}_i - \frac{|\dot{q}_i|}{g_2(\dot{q}_i)}z_{2i} \end{cases} \quad (8)$$

where z_{2i} and \dot{z}_{2i} denote the average bristle deformation amount and deformation rate of the low-speed axis, respectively. F_{c2i} , F_{s2i} , ω_{s2i} , $g_2(\dot{q}_i)$, respectively, denote the Coulomb friction, Stribeck friction, Stribeck velocity and static friction functions of low-speed shafts. σ_{02i} , σ_{12i} and σ_{22i} denote the bristle stiffness, bristle damping and viscous friction of the joint side, respectively. \dot{q}_i is the angular velocity of the robot joint.

Because the material, quality and lubrication conditions of the motor side and the joint side of the harmonic drive are almost all the same, the parameters of the LuGre model take the same values.

$$\begin{aligned} \sigma_{01i} = \sigma_{02i} = \sigma_{0i}, \sigma_{11i} = \sigma_{12i} = \sigma_{1i}, \sigma_{21i} = \sigma_{22i} = \sigma_{2i} \\ F_{c1i} = F_{c2i} = F_{ci}, F_{s1i} = F_{s2i} = F_{si}, \omega_{s1i} = \omega_{s2i} = \omega_{si} \end{aligned} \quad (9)$$

From Equation (1) to Equation (9), the generalized model of the robot joint servo system is deduced as

$$\bar{M}(q)\ddot{q} + \bar{C}(q, \dot{q})\dot{q} + \bar{G}(q) = \tau - \bar{F} - F_f \quad (10)$$

where

$$\bar{M}(q) = \eta M(q) + \eta^{-1}J_g + \eta J_d \quad (11)$$

$$\bar{C}(q, \dot{q}) = \eta C(q, \dot{q}) + \eta R_f \quad (12)$$

$$\bar{G}(q) = \eta G(q) \quad (13)$$

$$\bar{F} = \eta J^T F \quad (14)$$

$$F_f = \sigma_0[z_1 + \eta \cdot z_2] + \sigma_1[\dot{z}_1 + \eta \cdot \dot{z}_2] + \sigma_2(\eta^{-1} + \eta)\dot{q}. \quad (15)$$

The dynamic equation (Equation (10)) of the robot system satisfies the following properties [34].

1. $\bar{M}(q)$ is the positive definite symmetric matrix, and an inverse matrix $\bar{M}^{-1}(q)$ exists. $\bar{M}(q)$ and $\bar{M}^{-1}(q)$, as functions of q , are uniformly bounded. Namely, the existence of \bar{M}_{\min} and \bar{M}_{\max} makes the following equation hold:

$$0 < \bar{M}_{\min} \leq \bar{M}(q) \leq \bar{M}_{\max} \tag{16}$$

2. $\dot{\bar{M}}(q) - 2\bar{C}(q, \dot{q})$ is the skew symmetric matrix. Namely, $\forall x \in R^n$ can satisfy the following equation:

$$x^T (\dot{\bar{M}}(q) - 2\bar{C}(q, \dot{q})) x = 0 \tag{17}$$

3. Design of Optimized Cooperative Control

The control graph of the optimized cooperative control of a 2-DOF robot servo system is displayed in Figure 2. q_1, q_2 and q_1^*, q_2^* are the practical positions and expected positions of the robot joint, respectively. τ_{e1}, τ_{e2} are the output torque of the EPCH energy controller, τ_{s1}, τ_{s2} are the output torque of the ABSM signal controller, τ_1, τ_2 is the output torque after the application of optimized cooperative control, τ_{m1}, τ_{m2} are the electromagnetic torque of PMSM, and u_1, u_2 are the output voltage of PMSM. The inverter is a triphase inverter. Space Vector Pulse Width Modulation (SVPWM) is the pulse width modulation technology, which generates a pulse width modulation wave by switching mode. It considers the inverter system and PMSM as a whole, and the model is relatively simple.

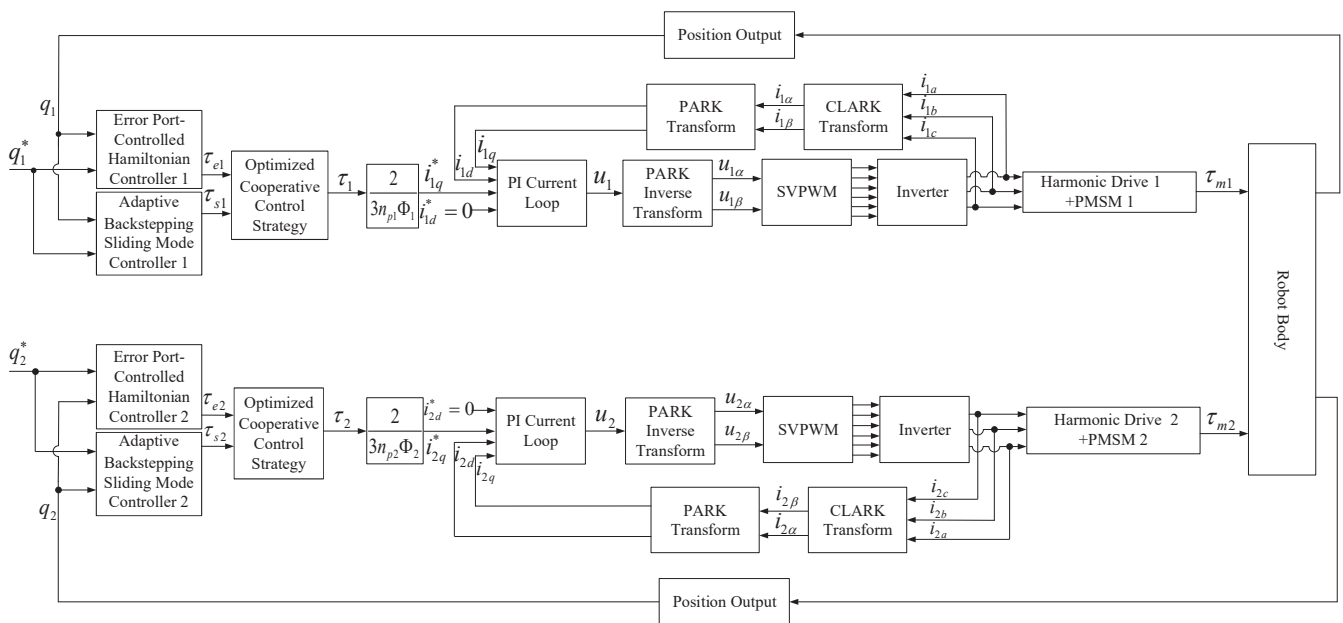


Figure 2. The control graph of optimized cooperative control of an EPCH energy controller and ABSM signal controller.

The PI current loop is designed as follows:

$$\begin{cases} u_{di} = \lambda_{pi}(i_{di}^* - i_{di}) + \lambda_{ii} \int (i_{di}^* - i_{di}) \\ u_{qi} = \lambda_{pi}(i_{qi}^* - i_{qi}) + \lambda_{ii} \int (i_{qi}^* - i_{qi}) \end{cases} \tag{18}$$

where $\lambda_{pi}, \lambda_{ii}$ are, respectively, the scale coefficient and integral coefficient of the PI current loop, which includes the adjustment of parameters L_{di}, L_{qi} and R_{si} .

Because the current loop adopts PI control, the PMSM parameters L_{di} , L_{qi} and R_{si} do not need to be adjusted, and only the parameters λ_{pi} and λ_{ii} of the PI current loop need to be adjusted.

3.1. Design of EPCH Energy Controller

For a nonlinear system, the PCH model of the EPCH energy controller with energy dissipation can be calculated as [35–38]

$$\begin{cases} \dot{x} = [J(x) - R(x)] \frac{\partial H(x)}{\partial x} + g(x)u \\ y = g^T(x) \frac{\partial H(x)}{\partial x} \end{cases} \quad (19)$$

where x , u , and y are the state vector, control vector, and output vector. $J(x)$ is the interconnection matrix, $J(x) = -J^T(x)$, which expresses the interconnection structure. $R(x)$ is the damping matrix, $R(x) = R^T(x) \geq 0$, which shows the resistive structure on the port. $g(x)$ reflects the port's characteristics. $H(x)$ is the Hamiltonian function, which signifies the total energy stored by the system.

The state vector, control vector and position error of the robot joints are defined, respectively, as

$$x = \begin{bmatrix} q \\ p \end{bmatrix} = \begin{bmatrix} I_{2 \times 2} & 0_{2 \times 2} \\ 0_{2 \times 2} & \bar{M}(q) \end{bmatrix} \begin{bmatrix} q \\ \dot{q} \end{bmatrix} \quad (20)$$

$$\tau_e = [\tau_{e1} \ \tau_{e2}]^T \quad (21)$$

$$\tilde{q} = q^* - q \quad (22)$$

where $p = \bar{M}(q)\dot{q}$ denotes the generalized inertia matrix of the system, and $q^* = [q_1^*, q_2^*]^T$ denotes the expected value of the robot joint's motion trajectory.

The Hamiltonian function $H(x)$ of robot joints is defined as

$$H(x) = \frac{1}{2} p^T \bar{M}^{-1}(q) p + V(q) \quad (23)$$

where $V(q)$ is the potential energy of the robot joints.

Taking the partial differentiation of Equation (23), we can get

$$\frac{\partial H(x)}{\partial x} = \begin{bmatrix} \frac{\partial H(x)}{\partial q} \\ \frac{\partial H(x)}{\partial p} \end{bmatrix} = \begin{bmatrix} \frac{1}{2} \dot{q}^T \frac{\partial \bar{M}(q)}{\partial q} \dot{q} \\ \bar{M}^{-1}(q) p \end{bmatrix} = \begin{bmatrix} \frac{1}{2} \dot{q}^T \frac{\partial \bar{M}(q)}{\partial q} \dot{q} \\ \dot{q} \end{bmatrix} \quad (24)$$

Using Equations (17) and (24), we have

$$\dot{p} = -\frac{\partial H(x)}{\partial q} + \tau_e \quad (25)$$

Then, combining Equations (19), (24) and (25), the PCH model of a 2-DOF robot is expressed as

$$\begin{cases} \dot{x} = [J(x) - R(x)] \frac{\partial H(x)}{\partial x} + g(x)\tau_e \\ y = \dot{q} \end{cases} \quad (26)$$

where

$$J(x) = -J^T(x) = \begin{bmatrix} 0_{2 \times 2} & I_{2 \times 2} \\ -I_{2 \times 2} & 0_{2 \times 2} \end{bmatrix} \quad (27)$$

$$R(x) = R^T(x) = \begin{bmatrix} \mathbf{0}_{2 \times 2} & \mathbf{0}_{2 \times 2} \\ \mathbf{0}_{2 \times 2} & \mathbf{0}_{2 \times 2} \end{bmatrix} \tag{28}$$

$$g(x) = \begin{bmatrix} \mathbf{0}_{2 \times 2} \\ I_{2 \times 2} \end{bmatrix} \tag{29}$$

Introducing state error into the PCH model can further improve the tracking accuracy of the system. The following is the design process of the EPCH controller.

The state error of the robot joints is

$$\tilde{x} = x^* - x = \begin{bmatrix} \tilde{q} \\ \tilde{p} \end{bmatrix} \tag{30}$$

where x^* is the expected state matrix.

The expected Hamiltonian function, including the kinetic energy and potential energy of the robot joint, is chosen as

$$H_d(\tilde{x}) = \frac{1}{2} \tilde{p}^T M_d^{-1} \tilde{p} + \frac{1}{2} \tilde{q}^T K_p \tilde{q} \tag{31}$$

where $M_d = M_d^T > 0$ denotes the moment of inertia, and $\frac{1}{2} \tilde{p}^T M_d^{-1} \tilde{p}$ indicates the kinetic energy of the robot joints. $K_p = K_p^T > 0$ denotes the proportional gain and $\frac{1}{2} \tilde{q}^T K_p \tilde{q}$ indicates the potential energy of robot joints.

Calculating the derivation of Equation (31), we have

$$\frac{\partial H_d(\tilde{x})}{\partial \tilde{x}} = \begin{bmatrix} \frac{\partial H_d(\tilde{x})}{\partial \tilde{q}} \\ \frac{\partial H_d(\tilde{x})}{\partial \tilde{p}} \end{bmatrix} = \begin{bmatrix} K_p \tilde{q} \\ M_d^{-1} \tilde{p} \end{bmatrix} \tag{32}$$

when the system is in equilibrium, that is, $\tilde{x} = 0$, the internal storage energy of the system is the smallest. At this time, the form of the EPCH is expressed as

$$\dot{\tilde{x}} = [J_d(\tilde{x}) - R_d(\tilde{x})] \frac{\partial H_d(\tilde{x})}{\partial \tilde{x}} \tag{33}$$

where the expected interconnection matrix $J_d(\tilde{x})$ and expected damping matrix $R_d(\tilde{x})$ are chosen as

$$J_d(\tilde{x}) = -J_d^T(\tilde{x}) = \begin{bmatrix} \mathbf{0}_{2 \times 2} & \bar{M}^{-1}(q) M_d \\ -M_d \bar{M}^{-1}(q) & \mathbf{0}_{2 \times 2} \end{bmatrix} \tag{34}$$

$$R_d(\tilde{x}) = R_d^T(\tilde{x}) = \begin{bmatrix} \mathbf{0}_{2 \times 2} & \mathbf{0}_{2 \times 2} \\ \mathbf{0}_{2 \times 2} & K_v \end{bmatrix} \tag{35}$$

The gain of damping matrix $K_v = K_v^T > 0$.
From Equations (26), (30) and (33), we can get

$$g(x) \tau_e = [J_d(\tilde{x}) - R_d(\tilde{x})] \frac{\partial H_d(\tilde{x})}{\partial \tilde{x}} - [J(x) - R(x)] \frac{\partial H(x)}{\partial x} + \dot{x}^*. \tag{36}$$

Using Equation (36), we can obtain the control law

$$\tau_e = -K_l \tilde{q} - K_t \dot{\tilde{q}} + \bar{C}(q, \dot{q}) \dot{\tilde{q}} + \bar{G}(q) + \bar{F} + F_f - \dot{\bar{M}}(q) \dot{\tilde{q}} \tag{37}$$

where $K_l = M_d \bar{M}^{-1}(q) K_p$, $K_t = M_d^{-1} \bar{M}(q) K_v$.

The desired Hamiltonian function (31) is the Lyapunov function, so the Lyapunov function V_e is

$$V_e = \frac{1}{2} \tilde{p}^T M_d^{-1} \tilde{p} + \frac{1}{2} \tilde{q}^T K_p \tilde{q} \tag{38}$$

From the derivation of Equation (38), we can obtain

$$\dot{V}_e = \tilde{p}^T M_d^{-1} \dot{\tilde{p}} + \tilde{q}^T K_p \dot{\tilde{q}} \tag{39}$$

Substituting Equations (10) and (37) into Equation (39), we can get

$$\dot{V}_e = - \left[M_d^{-1} \bar{M}(q) \dot{\tilde{q}} \right]^T K_v \left[M_d^{-1} \bar{M}(q) \dot{\tilde{q}} \right] \leq 0. \tag{40}$$

$\{x^*\}$ is the largest invariant set of $\left\{ \tilde{x}_r \in \mathfrak{R}^4 \mid \left[M_d^{-1} \bar{M}(q) \dot{\tilde{q}} \right]^T K_v \left[M_d^{-1} \bar{M}(q) \dot{\tilde{q}} \right] = 0 \right\}$. Therefore, according to the Lasalle invariant set principle, the closed-loop control system of the robot is asymptotically stable at the equilibrium point.

3.2. Design of ABSM Signal Controller

The EPCH energy controller has the advantages of high precision and strong stability. However, its dynamic properties are not ideal when it is used alone. Therefore, the ABSM signal controller is proposed to compensate for the dynamic properties.

Before the construction of the ABSM signal controller, it is required to improve the dynamic equation of the robot joint system. We need to replace the friction moment term F_f with the uncertainty term \bar{d} , and construct an adaptive law to estimate the uncertainty term \bar{d} in real time, that is, making $\bar{d} = F_f$. Then, Equation (10) is represented as

$$\bar{M}(q) \ddot{q} + \bar{C}(q, \dot{q}) \dot{q} + \bar{G}(q) = \tau - \bar{F} - \bar{d} \tag{41}$$

where \bar{d} only includes friction interference caused by PMSM, harmonic drive and the robot body, and any other external interference is not considered.

The design of the ABSM signal controller is as follows. Equation (41) is converted to a state space expression:

$$\begin{cases} \dot{x}_1 = x_2 = \dot{q} \\ \dot{x}_2 = \bar{M}^{-1}(q) [\tau - \bar{C}(q, \dot{q}) \dot{q} - \bar{G}(q) - \bar{F} - \bar{d}] \end{cases} \tag{42}$$

Step 1: The position error of the robot joints is defined as

$$\tilde{q} = q^* - q \tag{43}$$

where q^* denotes the desired position of the robot joint.

Taking the derivative of Equation (43), we get

$$\dot{\tilde{q}} = \dot{q}^* - \dot{q} \tag{44}$$

We take the virtual control quantity $\alpha_1 = c_1 \tilde{q}$ and define

$$\tilde{q}_1 = \dot{\tilde{q}} + \alpha_1 \tag{45}$$

The Lyapunov function of the subsystem of Step 1 is selected as

$$V_1 = \frac{1}{2} \tilde{q}^T \tilde{q} \tag{46}$$

We conduct the derivative of Equation (46) and use Equation (45) to obtain

$$\dot{V}_1 = \tilde{q}^T \dot{\tilde{q}} = \tilde{q}^T (\tilde{q}_1 - \alpha_1) = \tilde{q}^T \tilde{q}_1 - \tilde{q}^T c_1 \tilde{q} \tag{47}$$

In Equation (47), if $\tilde{q}_1 = 0$, then $\dot{V}_1 = -\tilde{q}^T c_1 \tilde{q} \leq 0$. Therefore, the next step of the design is needed.

Step 2: Taking the derivative of Equation (44) and using Equation (42), we get

$$\begin{aligned} \ddot{\tilde{q}} &= \dot{\tilde{q}}^* - \ddot{q} \\ &= \dot{\tilde{q}}^* - \bar{M}^{-1}(q) [\tau - \bar{C}(q, \dot{q})\dot{q} - \bar{G}(q) - \bar{F} - \bar{d}] \end{aligned} \tag{48}$$

The sliding surface of a traditional SMC is selected as

$$s = \beta \tilde{q} + \dot{\tilde{q}} \tag{49}$$

where β denotes the positive constant value matrix.

By calculating the derivative of Equation (49) and using Equation (42), we have

$$\begin{aligned} \dot{s} &= \beta \dot{\tilde{q}} + \ddot{\tilde{q}} \\ &= \beta \dot{\tilde{q}} + \dot{\tilde{q}}^* - \bar{M}^{-1}(q) [\tau - \bar{C}(q, \dot{q})\dot{q} - \bar{G}(q) - \bar{F} - \bar{d}] \end{aligned} \tag{50}$$

We define the Lyapunov function of subsystem of Step 2 as

$$V_2 = V_1 + \frac{1}{2} s^T s \tag{51}$$

We conduct the derivative of Equation (51) and combine Equations (47) and (50) to obtain

$$\begin{aligned} \dot{V}_2 &= \dot{V}_1 + s^T \dot{s} \\ &= \tilde{q}^T \tilde{q}_1 - \tilde{q}^T c_1 \tilde{q} + s^T (\beta \dot{\tilde{q}} + \dot{\tilde{q}}^* - \bar{M}^{-1}(q) [\tau - \bar{C}(q, \dot{q})\dot{q} - \bar{G}(q) - \bar{F} - \bar{d}]) \end{aligned} \tag{52}$$

The estimation error is defined as

$$\tilde{\tilde{d}} = \bar{d} - \hat{\tilde{d}} \tag{53}$$

where $\hat{\tilde{d}}$ is the estimated value of the uncertainty term \bar{d} , and $\dot{\hat{\tilde{d}}} = 0$.

Based on Equation (51), the Lyapunov function is defined at this time as

$$V_3 = V_2 + \frac{1}{2\delta} \tilde{\tilde{d}}^T \tilde{\tilde{d}} \tag{54}$$

where δ is the normal number matrix.

By taking the derivative of Equation (54), and combining Equation (52) with Equation (53), we can get

$$\begin{aligned} \dot{V}_3 &= \dot{V}_2 + \frac{1}{\delta} \tilde{\tilde{d}}^T \cdot \dot{\tilde{\tilde{d}}} = \dot{V}_2 - \frac{1}{\delta} \tilde{\tilde{d}}^T \cdot \dot{\hat{\tilde{d}}} \\ &= \tilde{q}^T \tilde{q}_1 - \tilde{q}^T c_1 \tilde{q} + s^T (\beta \dot{\tilde{q}} + \dot{\tilde{q}}^* \\ &\quad - \bar{M}^{-1}(q) [\tau - \bar{C}(q, \dot{q})\dot{q} - \bar{G}(q) - \bar{F} - \bar{d}]) - \frac{1}{\delta} \tilde{\tilde{d}}^T \cdot \dot{\hat{\tilde{d}}} \\ &= \tilde{q}^T \tilde{q}_1 - \tilde{q}^T c_1 \tilde{q} + s^T (\beta \dot{\tilde{q}} + \dot{\tilde{q}}^* \\ &\quad - \bar{M}^{-1}(q) [\tau - \bar{C}(q, \dot{q})\dot{q} - \bar{G}(q) - \bar{F} - \tilde{\tilde{d}} - \hat{\tilde{d}}]) - \frac{1}{\delta} \tilde{\tilde{d}}^T \cdot \dot{\hat{\tilde{d}}} \\ &= \tilde{q}^T \tilde{q}_1 - \tilde{q}^T c_1 \tilde{q} + s^T (\beta \dot{\tilde{q}} + \dot{\tilde{q}}^* \\ &\quad - \bar{M}^{-1}(q) [\tau - \bar{C}(q, \dot{q})\dot{q} - \bar{G}(q) - \bar{F} - \hat{\tilde{d}}]) - \frac{1}{\delta} \tilde{\tilde{d}}^T \cdot \dot{\hat{\tilde{d}}} + s \bar{M}^{-1}(q) \tilde{\tilde{d}} \\ &= \tilde{q}^T \tilde{q}_1 - \tilde{q}^T c_1 \tilde{q} + s^T (\beta \dot{\tilde{q}} + \dot{\tilde{q}}^* \\ &\quad - \bar{M}^{-1}(q) [\tau - \bar{C}(q, \dot{q})\dot{q} - \bar{G}(q) - \bar{F} - \hat{\tilde{d}}]) - \frac{1}{\delta} \tilde{\tilde{d}}^T (\dot{\hat{\tilde{d}}} - \delta \bar{M}^{-1}(q) s) \end{aligned} \tag{55}$$

In order to simplify Equation (55) and further prove $\dot{V}_3 \leq 0$, the control torque of the robot joint is selected

$$\tau = \bar{M}(q)(\beta\dot{\tilde{q}} + \ddot{q}^* + \rho s + \lambda\rho \operatorname{sgn} s) + \bar{C}(q, \dot{q})\dot{q} + \bar{G}(q) + \bar{F} + \hat{d} \tag{56}$$

where ρ is the symmetric and positive constant value matrix, and λ is a normal number. The adaptive law can be taken as

$$\dot{\hat{d}} = \delta \bar{M}^{-1}(q)s. \tag{57}$$

The Lyapunov function of the whole robot system is defined as

$$V_3 = \frac{1}{2}\tilde{q}^T\tilde{q} + \frac{1}{2}s^T s + \frac{1}{2\delta}\tilde{d}^T\tilde{d}. \tag{58}$$

By taking the derivative of Equation (58), and substituting Equations (56) and (57) into Equation (55), we get

$$\dot{V}_3 = \tilde{q}^T\dot{\tilde{q}}_1 - \tilde{q}^T c_1\tilde{q} - s^T \rho s - \sum_{j=1}^2 \sum_{i=1}^2 \lambda \rho_{ij} |s_i|. \tag{59}$$

We take $T = \begin{bmatrix} c_1 + \beta^T \rho \beta & \rho \beta - \frac{I}{2} \\ \rho \beta - \frac{I}{2} & \rho \end{bmatrix}$, and take the appropriate value to turn T into the positive definite matrix. We have $\eta = [\tilde{q}^T \ \tilde{q}_1^T]$, and get

$$\eta^T T \eta = [\tilde{q}^T \ \tilde{q}_1^T] \begin{bmatrix} c_1 + \beta^T \rho \beta & \rho \beta - \frac{I}{2} \\ \rho \beta - \frac{I}{2} & \rho \end{bmatrix} \begin{bmatrix} \tilde{q} \\ \tilde{q}_1 \end{bmatrix} = \tilde{q}^T c_1 \tilde{q} - \tilde{q} \tilde{q}_1 + s^T \rho s. \tag{60}$$

Namely,

$$\dot{V}_3 = -\eta^T T \eta - \sum_{j=1}^2 \sum_{i=1}^2 \lambda \rho_{ij} |s_i| \leq 0. \tag{61}$$

With the design of the above controller, the sliding surface can ultimately be bounded as stable, and the robot joints can move according to the desired trajectory.

3.3. Strategy of Optimized Cooperative Control

3.3.1. Design of Optimized Cooperative Controller

The ABSM signal controller contributes rapid response speed and outstanding dynamic performance to the system; the EPCH energy controller generates high tracking precision and impressive steady-state behavior. The strategy of optimized cooperative control is designed to combine the advantages of these two controllers. Additionally, the coefficient matrix of optimized cooperative control $h(\tilde{q})$ is introduced in order to make the control vector change continuously and smoothly in the optimized cooperative control procedure.

The design of the optimized cooperative controller is calculated as

$$\tau = h(\tilde{q}) \cdot \tau_e(\tilde{q}) + [I - h(\tilde{q})] \cdot \tau_s(\tilde{q}) \tag{62}$$

where τ denotes the input torque of a joint after optimized cooperative control, $h(\tilde{q})$ is the coefficient matrix of optimized cooperative control based on the position error of the robot joint, and $h(\tilde{q}) = \operatorname{diag}\{h(\tilde{q}_1), h(\tilde{q}_2)\}$.

There are many kinds of mathematical function that can be used as cooperative control coefficients, and different cooperative control coefficients have different effects on the cooperative control of the system. In order to study which coefficient has the best effect

on the cooperative control of the system, four kinds of cooperative control coefficient, namely a Gaussian function, hyperbolic tangent function, arctangent function, and Cauchy distribution function, are selected for comparison. Additionally, the optimized cooperative control coefficient is determined through comparative analysis of the scale effect, switching accuracy, switching speed and storage space.

The specific forms of the four cooperative control coefficients are shown in Table 1, where $h(\tilde{q})$, $f(\tilde{q})$, $k(\tilde{q})$ and $g(\tilde{q})$ represent the Gaussian function, hyperbolic tangent function, arctangent function and Cauchy distribution function, respectively, and σ represents the scale parameters.

Table 1. The forms of cooperative control coefficients.

Function	Function Name	Function Form
$h(\tilde{q})$	Gaussian function	$e^{-\left(\frac{\tilde{q}_i}{\sigma}\right)^2}$
$f(\tilde{q})$	Hyperbolic tangent function	$1 - \frac{e^{\left(\frac{\tilde{q}_i}{\sigma}\right)^2} - e^{-\left(\frac{\tilde{q}_i}{\sigma}\right)^2}}{e^{\left(\frac{\tilde{q}_i}{\sigma}\right)^2} + e^{-\left(\frac{\tilde{q}_i}{\sigma}\right)^2}}$
$k(\tilde{q})$	Arctangent function	$1 - \frac{2}{\pi} \arctan\left(\frac{\tilde{q}_i}{\sigma}\right)^2$
$g(\tilde{q})$	Cauchy distribution function	$\frac{1}{1 + \pi\left(\frac{\tilde{q}_i}{\sigma}\right)^2}$

Because the different scale parameters directly affect the cooperative control effect, it is important to carry out an analysis of parameter selection. When a scale parameter $\sigma > 1$ is adopted, the tracking curve after the cooperative control is similar to that of the EPCH controller used alone, and the system’s rapidity is poor at this time; when a scale parameter $0.01 < \sigma < 1$ is adopted, the system’s rapidity gradually improves with the decrease of the scale parameter σ ; when a scale parameter $\sigma < 0.01$ is adopted, the system’s rapidity is almost unchanged with the decrease of scale parameter σ . In order to give the system good dynamic performance, and taking into account the factor of computational complexity, four groups of parameters $\sigma = 0.01$, $\sigma = 0.05$, $\sigma = 0.1$, and $\sigma = 0.5$ are selected and analyzed. The mathematical curves of the above four coefficients are displayed in Figure 3, where $e = \tilde{q}$.

It can be seen from Figure 3 that, with a given scale parameter, the distribution trends of the four control coefficients are the same. Therefore, the scale effects are the same. Additionally, the function curves change mainly around the zero value; hence, the EPCH energy controller and ABSM signal controller start to switch when the error approaches zero. It can also be seen that the trend of the hyperbolic tangent function curve is steeper; the trend of the Gaussian function curve is steep; the trend of the arctangent function curve is gentler; and the Cauchy distribution function’s curve is gentle. The steeper the curve changes around zero value, the faster the switching process is completed, the higher the switching accuracy, and the faster and more accurate the system is. However, the algorithmic complexity of the four cooperative control coefficients are different, so the switching speed and storage space are also different. The higher the complexity of the algorithm, the slower the switching speed and the larger the storage space. On the contrary, the faster the switching speed, the smaller the storage space occupied.

To sum up, the scale effects are the same when any of the above four cooperative control coefficients are adopted. The steeper the curve, the higher the switching accuracy; the higher the complexity of the algorithm, the slower the switching speed, and the larger the storage space occupied. Table 2 presents a comprehensive comparison of the four kinds of cooperative control coefficient.

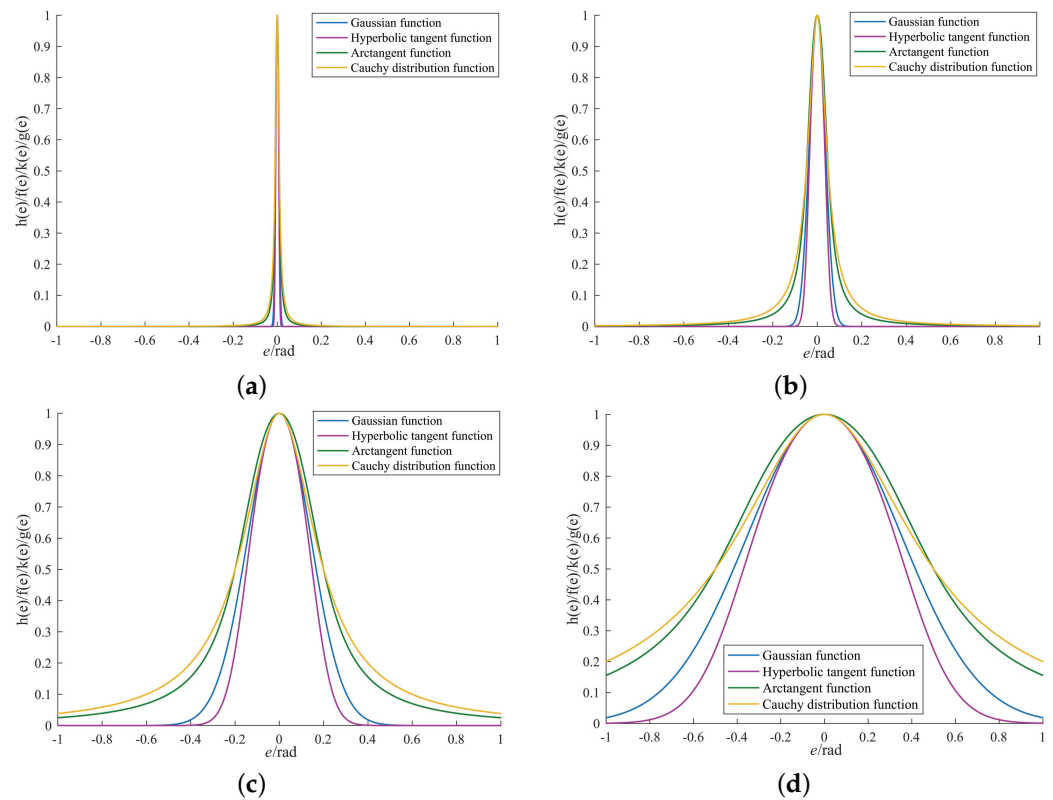


Figure 3. Mathematical curves of four cooperative control coefficients under different scale parameters. (a) The curves of four kinds of cooperative control coefficient with $\sigma = 0.01$. (b) The curves of four kinds of cooperative control coefficient with $\sigma = 0.05$. (c) The curves of four kinds of cooperative control coefficient with $\sigma = 0.1$. (d) The curves of four kinds of cooperative control coefficient with $\sigma = 0.5$.

Table 2. The form of cooperative control coefficients.

Function	Scale Effect	Switching Precision	Switching Speed	Storage Space	Comprehensive Comparison
$h(e)$	same	better	faster	less	best
$f(e)$	same	best	slowest	largest	better
$k(e)$	same	poor	slower	larger	poor
$g(e)$	same	worst	fastest	least	worst

Through the comparison and analysis of scale effect, switching precision, switching speed and storage space, it is shown that the Gaussian function has the best effect on the cooperative control. Therefore, the Gaussian function is the optimized cooperative control coefficient and is used in the strategy of optimized cooperative control, as shown:

$$h(\tilde{q}) = e^{-\left(\frac{\tilde{q}}{\sigma}\right)^2} \tag{63}$$

In order to illustrate the process of optimized cooperative control, the relationship curves between optimized cooperative control coefficient $h(\tilde{q})$ and position error \tilde{q} are shown in Figure 4, where $e = \tilde{q}$.

3.3.2. Stability Proof of the Overall Robot System with Optimized Cooperative Control

Case 1: When $\tilde{q}_i \rightarrow \infty$, that is $h(\tilde{q}_i) \rightarrow 0$, according to Equation (62), $\tau = \tau_s(\tilde{q})$. Only the ABSM signal controller works at this time, and the overall system of the robot is asymptotically stable.

Case 2: When $\tilde{q}_i = 0$, that is $1 - h(\tilde{q}_i) = 0$, according to Equation (62), $\tau = \tau_e(\tilde{q})$. Only the EPCH energy controller works at this time, and the overall system of the robot is asymptotically stable.

Case 3: When $0 < \tilde{q}_i < \infty$, that is $0 < h(\tilde{q}_i) < 1$, $0 < 1 - h(\tilde{q}_i) < 1$, according to Equation (62), $\tau = \tau_s(\tilde{q}) + \tau_e(\tilde{q})$. In this case, the EPCH energy controller and ABSM signal controller work together. The Lyapunov function of the overall robot system is defined as:

$$V = V_e + V_3 > 0. \tag{64}$$

By taking the derivative of Equation (64) and combining Equations (40) and (61), we can get

$$\dot{V} = \dot{V}_e + \dot{V}_3 \leq 0. \tag{65}$$

According to the Lasalle invariant set principle, the overall robot system is asymptotically stable. Consequently, the overall robot system after the application of optimized cooperative control is asymptotically stable.

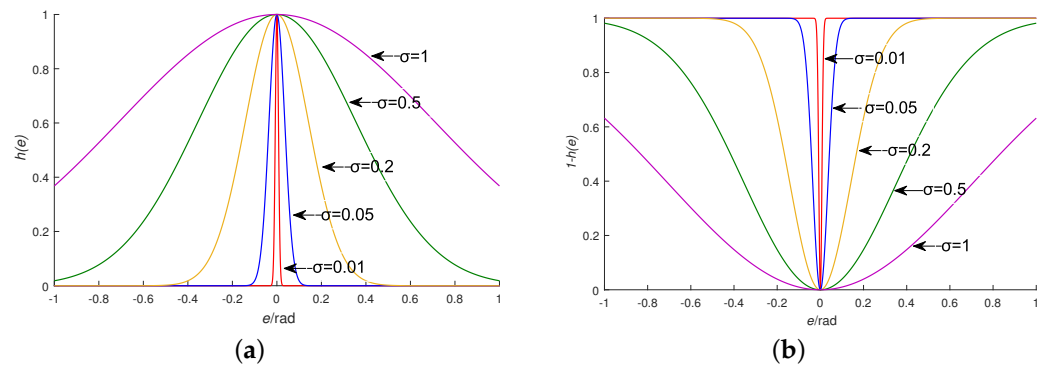


Figure 4. The curves of optimized cooperative control coefficient. (a) The function curve of $h(\tilde{q})$. (b) The function curve of $1 - h(\tilde{q})$.

4. Simulation Results

To demonstrate the validity of the optimized cooperative control method, Joint 1 and Joint 2 are taken as an example to simulate and analyze the robot system. The parameters of the EPCH energy controller are: $K_I = \text{diag}\{50000, 50000\}$, $K_t = \text{diag}\{3000, 3000\}$. The parameters of the ABSM signal controller are: $\beta = \text{diag}\{50, 50\}$, $\rho = \text{diag}\{200, 200\}$, $\lambda = 5$, $\delta = \text{diag}\{30, 30\}$. The parameters of the PI current loop are: $\lambda_{pi} = 5$, $\lambda_{ii} = 10$. The scale parameter is $\sigma = \text{diag}\{0.01, 0.01\}$. The parameters of PMSM and the LuGre model are displayed in Table 3.

Table 3. Parameters of PMSM and LuGre model.

Symbol	Quantity	Values	Unit
Φ_i	rotor flux	0.29	Wb
J_{mi}	moment of inertia	0.03	kg·m ²
n_{pi}	number of pole-pairs	4	-
F_{ci}	Coulomb friction	0.649	N·m
F_{si}	Stribeck friction	0.684	N·m
ω_{si}	Stribeck velocity	0.02	rad/s
σ_{0i}	bristle stiffness	45.01	-
σ_{1i}	bristle damping	1.28	-
σ_{2i}	viscous friction	0.171	-

Case 1: To verify the advantage of the ABSM signal controller in dynamic response performance, simulations are conducted to compare the ABSM controller with BC, SMC, and feedback linearization control (FLC). Under no load condition, Joint 1 and Joint 2 track the unit step signal. The simulation results are shown in Figure 5. The results indicate that the ABSM controller has the fastest dynamic response speed among the above four controllers. Therefore, the ABSM controller is the most suitable as the signal controller in the strategy of optimized cooperative control. The performance index of the four controllers is shown in Table 4. It can be seen from Table 4 that dynamic response time is the shortest when the ABSM controller is adopted.

Table 4. Performance index of ABSM, BC, SMC, and FLC with unit step response.

Description	ABSM	BC	SMC	FLC
Joint 1: rise time	0.13 s	0.14 s	0.35 s	0.39 s
Joint 2: rise time	0.12 s	0.15 s	0.31 s	0.42 s

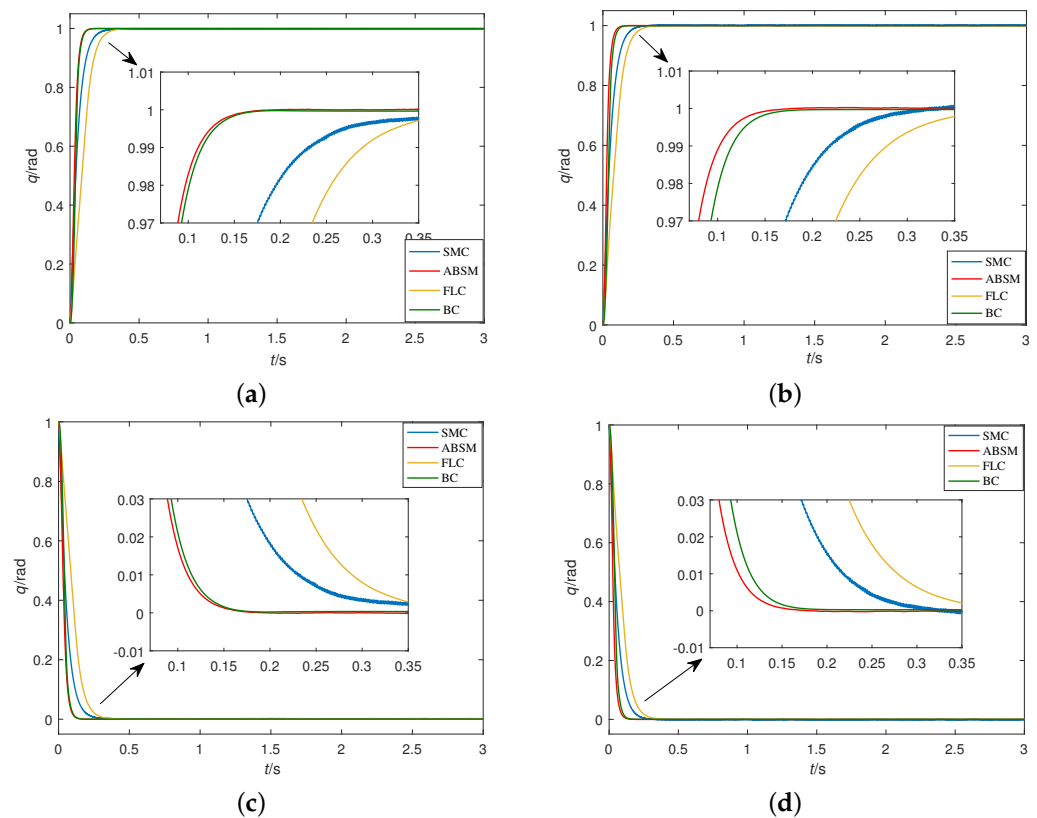


Figure 5. Position tracking curve and tracking error curve of two joints under ABSM, BC, SMC, and FLC. (a) Position tracking curve of Joint 1. (b) Position tracking curve of Joint 2. (c) Tracking error curve of Joint 1. (d) Tracking error curve of Joint 2.

Case 2: To prove the effect of scale parameters on the cooperative control performance of the system, we select four groups of parameters: $\sigma = 0.01$, $\sigma = 0.05$, $\sigma = 0.1$ and $\sigma = 0.5$. Robot joints track the unit step signal under the above four groups of parameters. The simulation results are shown in Figure 6. It can be observed from Figure 6 that the response speed of the system is the fastest with $\sigma = 0.01$. The steady-state error rates of the system are the same with different scale parameters. Furthermore, the smaller the scale parameter, the faster the response speed. Therefore, we choose the scale parameter $\sigma = 0.01$ in the following Case 3. In this case, the dynamic characteristics of the robot servo system are optimal.

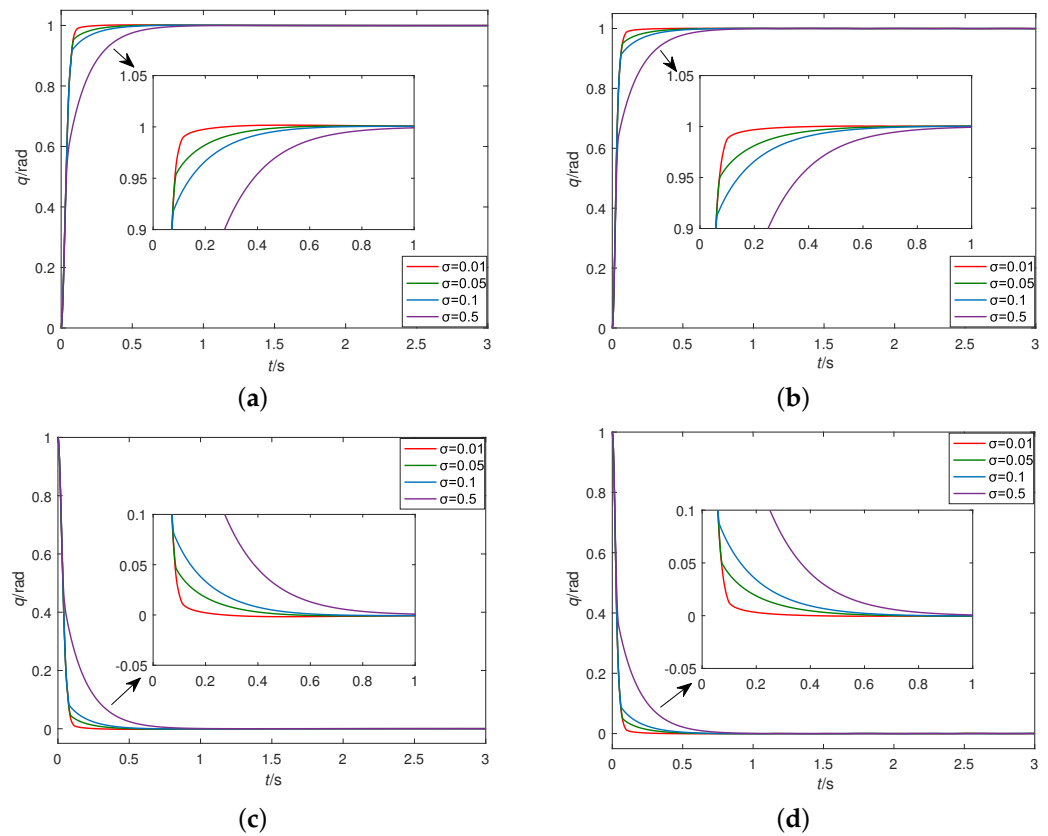


Figure 6. Position tracking curve and tracking error curve of two joints with different scale parameters. (a) Position tracking curve of Joint 1. (b) Position tracking curve of Joint 2. (c) Tracking error curve of Joint 1. (d) Tracking error curve of Joint 2.

Case 3: To demonstrate the effectiveness of the strategy of optimized cooperative control, the curve of unit step response is measured. The scale parameter is set to $\sigma = \text{diag}\{0.01, 0.01\}$. The obtained curves of position tracking are displayed in Figure 7. The simulation results reveal that the control characteristic after the application of optimized cooperative control is significantly better than with EPCH or ABSM. It can be seen from Table 5 that, when the ABSM signal controller is used alone, the rise time of the system is about (0.17 s, 0.18 s) and the tracking error of the system is about (± 0.0025 rad, ± 0.0018 rad); when the EPCH controller is used alone, the system’s rise time is about (1.02 s, 1.06 s) and its tracking error is about (± 0.0004 rad, ± 0.0004 rad); when the strategy of optimized cooperative control is used, the system’s rise time is about (0.21 s, 0.23 s) and its tracking error is about (± 0.0004 rad, ± 0.0004 rad). Therefore, the strategy of optimized cooperative control can reduce the rise time of the EPCH energy controller and the steady-state error of the ABSM signal controller. The optimized cooperative controller can give robot joints both superior rapidity and accuracy at once.

Table 5. Property indicators of EPCH, ABSM, and optimized cooperative control with unit step response.

Description	EPCH	ABSM	Optimized Cooperative Control
Joint 1: rise time (s)	1.02	0.17	0.21
tracking error (rad)	± 0.0004	± 0.0025	± 0.0004
Joint 2: rise time (s)	1.06	0.18	0.23
tracking error (rad)	± 0.0004	± 0.0018	± 0.0004

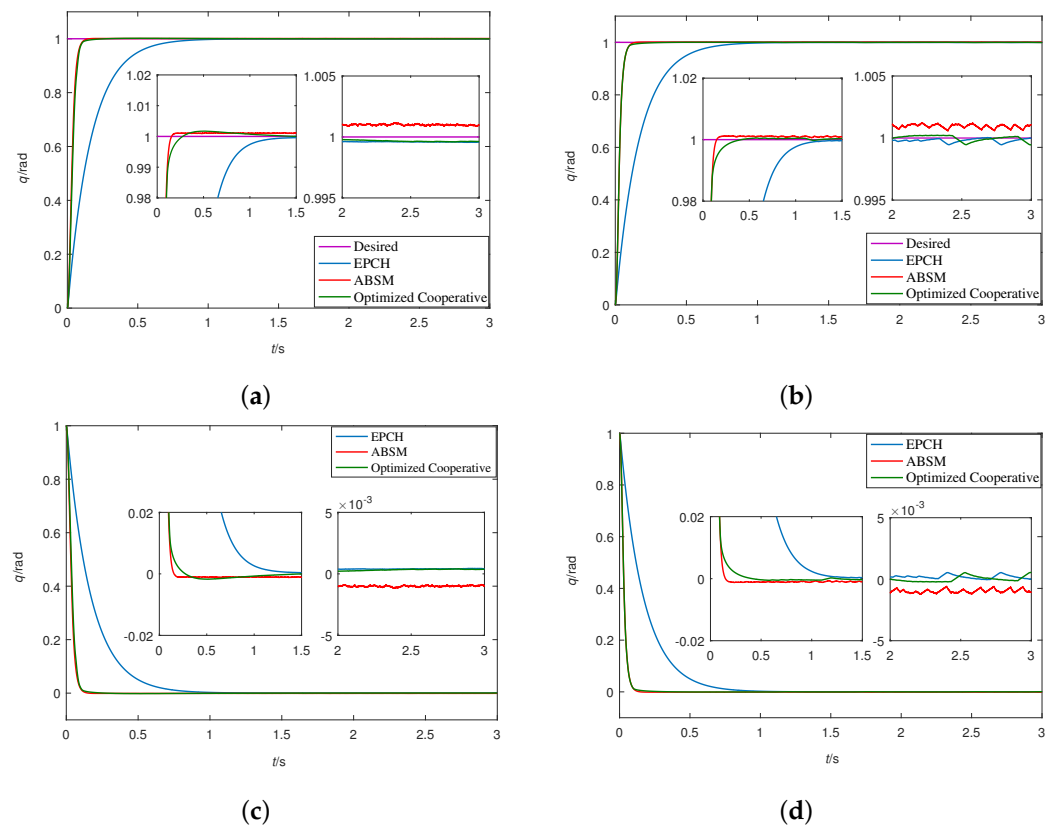


Figure 7. Position tracking curve and tracking error curve of two joints under the three control methods. (a) Position tracking curve of Joint 1. (b) Position tracking curve of Joint 2. (c) Tracking error curve of Joint 1. (d) Tracking error curve of Joint 2.

Case 4: To verify the influence of the PMSM mathematical model parameter Φ_i on the simulation results, the relevant parameter sensitivity analysis is shown in Figure 8. The robot joint with optimized cooperative control tracks the unit step signal. The rise time required by the system is the lowest when $\Phi_i = 0.29 \pm 0.01$ is selected; in this case, the system has the fastest dynamic response speed. However, a different PMSM mathematical model parameter Φ_i has almost the same effect on tracking error. Therefore, the system has the best control effect when $\Phi_i = 0.29$ is adopted and the approximate error is 0.01 about Φ_i .

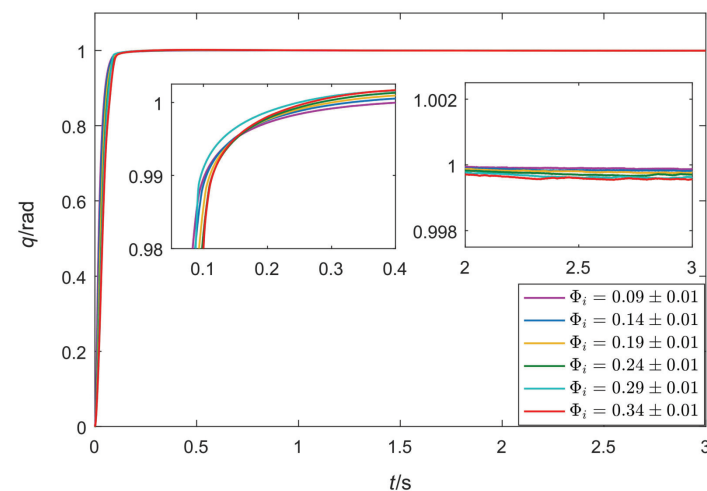


Figure 8. The parameter sensitivity analysis of Φ_i .

5. Conclusions

With the aim of improving the position control of PMSM-driven robot joints, the strategy of optimized cooperative control based on an EPCH energy controller and an ABSM signal controller is proposed. To enable smooth switching between the ABSM signal controller and EPCH energy controller, a Gaussian function based on the position error of robot joints is used as the optimized cooperative control coefficient. The simulation results show that, compared with BC, SMC and FLC, the ABSM signal controller can offer excellent dynamic performance for systems. Additionally, the rise times of Joint 1 and Joint 2 are 0.13 s and 0.12 s, respectively, when the ABSM signal controller is adopted. The optimized cooperative control effect of the robot system is at its best when $\sigma = 0.01$ is selected. The proposed optimized cooperative control strategy reduces rise time by about 79.4% compared with the ABSM signal controller and reduces tracking error by about 84% compared with the EPCH energy controller. Thus, the effectiveness of optimized cooperative control based on an EPCH energy controller and an ABSM signal controller is verified.

Author Contributions: The design of experimental methods, analysis of experimental data and writing the first draft of the paper were performed by X.Y. The supervision and guidance of the research projects, and the review and revision of papers were performed by H.Y. All authors have read and agreed to the published version of the manuscript.

Funding: The above work is sustained by the National Natural Science Foundation of China (62273189) and Natural Science Foundation of Shandong Province (ZR2021MF005).

Data Availability Statement: Not applicable.

Conflicts of Interest: On behalf of all authors, the corresponding author states that there are no conflict of interest.

Abbreviations

The following abbreviations are used in this manuscript:

- PMSM Permanent magnet synchronous motors
- EPCH Error port-controlled Hamiltonian
- ABSM Adaptive backstepping sliding mode
- DOF Degree of freedom
- BC Backstepping control
- SMC Sliding mode control
- PCH Port-controlled Hamiltonian
- FLC Feedback linearization control

Appendix A

The parameters in Lagrange’s equation of robot body are as follows:

$$M(q) = \begin{bmatrix} (m_1 + m_2)d_1^2 + m_2d_2^2 + 2m_2d_1d_2 \cos(q_2) & m_2d_2^2 + m_2d_1d_2 \cos(q_2) \\ m_2d_2^2 + m_2d_1d_2 \cos(q_2) & m_2d_2^2 \end{bmatrix} \tag{A1}$$

$$C(q, \dot{q}) = \begin{bmatrix} -2m_2d_1d_2\dot{q}_2 \sin(q_2) & -m_2d_1d_2\dot{q}_2 \sin(q_2) \\ m_2d_1d_2\dot{q}_1 \sin(q_2) & 0 \end{bmatrix} \tag{A2}$$

$$G(q) = \begin{bmatrix} (m_1 + m_2)gd_1 \sin(q_1) + m_2gd_2 \sin(q_1 + q_2) \\ m_2gd_2 \sin(q_1 + q_2) \end{bmatrix} \tag{A3}$$

$$R_f = \begin{bmatrix} 0.03 & 0 \\ 0 & 0.03 \end{bmatrix} \tag{A4}$$

$$J = [d_1 \cos(q_1) + d_2 \cos(q_1 + q_2) \quad d_2 \cos(q_1 + q_2)] \quad (\text{A5})$$

where $m_1 = m_2 = 0.5$, $d_1 = d_2 = 1$, and $g = 9.8$. q_1 and q_2 are the actual positions of Joint 1 and Joint 2. \dot{q}_1 and \dot{q}_2 are the actual velocities of Joint 1 and Joint 2.

References

1. Yang, L.; Huan, Z.; Han, D. External force estimation for industrial robots with flexible joints. *IEEE Robot. Autom. Lett.* **2020**, *5*, 1311–1318.
2. Rubio, J.; Orozco, E.; Cordova, D.A.; Islas, M.A. Modified linear technique for the controllability and observability of robotic arms. *IEEE Access* **2022**, *10*, 3366–3377. [[CrossRef](#)]
3. Soriano, L.A.; Rubio, J.D.; Orozco, E.; Cordova, D.A.; Ochoa, G. Optimization of sliding mode control to save energy in a SCARA robot. *Mathematics* **2021**, *9*, 3160. [[CrossRef](#)]
4. Liu, X.M.; You, B.D.; Wang, R.; Wen, J.M.; An, D.X.; Wen, X.L. Climbing strategy of variable topology cellular space robots considering configuration optimization. *Mathematics*. **2023**, *11*, 1410. [[CrossRef](#)]
5. Hong, D.K.; Hwang, W.; Lee, J.Y.; Woo, B.C. Design, analysis, and experimental validation of a permanent magnet synchronous motor for articulated robot applications. *IEEE Trans. Magn.* **2018**, *54*, 8201304. [[CrossRef](#)]
6. Schluter, M.D.; Perondi, E.A. Mathematical modeling with friction of SCARA robot driven by pneumatic semirotary actuators. *IEEE Lat. Am. Trans.* **2020**, *18*, 1066–1076. [[CrossRef](#)]
7. Zhang, W.J.; Li, M.Y.; Gao, Y.P.; Chen, Y.Q. Periodic adaptive learning control of PMSM servo system with LuGre model-based friction compensation. *Mech. Mach. Theory* **2022**, *167*, 104561. [[CrossRef](#)]
8. Yue, F.F.; Li, X.F. Robust adaptive integral backstepping control for opto-electronic tracking system based on modified LuGre friction model. *ISA Trans.* **2018**, *80*, 312–321. [[CrossRef](#)]
9. Dirks, D.A.; Scherpen, J.M.A. On tracking control of rigid-joint robots with only position measurements. *IEEE Trans. Control Syst. Technol.* **2013**, *21*, 1510–1513. [[CrossRef](#)]
10. Lu, W.Q.; Li, Q.; Lu, K.Y. Load adaptive PMSM drive system based on an improved ADRC for manipulator joint. *IEEE Access* **2021**, *9*, 33369–33384. [[CrossRef](#)]
11. Wai, R.J.; Muthusamy, R. Fuzzy-neural-network inherited sliding-mode control for robot manipulator including actuator dynamics. *IEEE Trans. Neural Netw. Learn. Syst.* **2013**, *24*, 274–287.
12. Sariyildiz, E.; Sekiguchi, H.; Nozaki, T. A stability analysis for the acceleration-based robust position control of robot manipulators via disturbance observer. *IEEE/ASME Trans. Mechatron.* **2018**, *23*, 2369–2378. [[CrossRef](#)]
13. Petrovic, V.; Ortega, R.; Stankovic, A.M. Interconnection and damping assignment approach to control of PM synchronous motors. *IEEE Trans. Control Syst. Technol.* **2001**, *9*, 811–820. [[CrossRef](#)]
14. Donaire, A.; Romero, J.G.; Ortega, R. A robust IDA-PBC approach for handling uncertainties in underactuated mechanical systems. *IEEE Trans. Autom. Control* **2020**, *65*, 3223–3226. [[CrossRef](#)]
15. Zheng, X.L.; Yang, X.B. Command filter and universal approximator based backstepping control design for strict-feedback nonlinear systems with uncertainty. *IEEE Trans. Autom. Control* **2020**, *65*, 1310–1317. [[CrossRef](#)]
16. Qiao, N.; Wang, L.H.; Liu, M.J.; Wang, Z.X. The sliding mode controller with improved reaching law for harvesting robots. *J. Intell. Robot. Syst.* **2022**, *104*, 9. [[CrossRef](#)]
17. Ling, S.; Wang, H.Q.; Liu, P.X. Adaptive fuzzy tracking control of flexible-joint robots based on command filtering. *IEEE Trans. Ind. Electron.* **2020**, *67*, 4046–4055. [[CrossRef](#)]
18. Jin, M.L.; Kang, S.H.; Chang, P.H.; Lee, J. Robust control of robot manipulators using inclusive and enhanced time delay control. *IEEE/ASME Trans. Mechatron.* **2017**, *22*, 2141–2152. [[CrossRef](#)]
19. Costa, T.L.; Lara-Molina, F.A.; Cavalini, A.A.; Taketa, E. Robust control H_∞ of computed torque for manipulators. *IEEE Lat. Am. Trans.* **2018**, *16*, 398–407. [[CrossRef](#)]
20. Pezzato, C.; Ferrari, R.; Corbato, C.H. A novel adaptive controller for robot manipulators based on active inference. *IEEE Robot. Autom. Lett.* **2020**, *5*, 2973–2980. [[CrossRef](#)]
21. Pan, Y.P.; Wang, H.M.; Li, X.; Yu, H.Y. Adaptive command-filtered backstepping control of robot arms with compliant actuators. *IEEE Trans. Control Syst. Technol.* **2018**, *26*, 1149–1156. [[CrossRef](#)]
22. Cheng, X.; Zhang, Y.J.; Liu, H.S.; Wollherr, D.; Buss, M. Adaptive neural backstepping control for flexible-joint robot manipulator with bounded torque inputs. *Neurocomputing* **2021**, *458*, 70–86. [[CrossRef](#)]
23. Lee, J.; Chang, P.H.; Jin, M.L. Adaptive integral sliding mode control with time-delay estimation for robot manipulators. *IEEE Trans. Ind. Electron.* **2017**, *64*, 6796–6804. [[CrossRef](#)]
24. Ren, C.; Li, X.H.; Yang, X.B.; Ma, S.G. Extended state observer-based sliding mode control of an omnidirectional mobile robot with friction compensation. *IEEE Trans. Ind. Electron.* **2019**, *66*, 9480–9489. [[CrossRef](#)]
25. Van, M.; Mavrouniotis, M.; Ge, S.S. An adaptive backstepping nonsingular fast terminal sliding mode control for robust fault tolerant control of robot manipulators. *IEEE Trans. Syst. Man Cybern. Syst.* **2019**, *49*, 1448–1458. [[CrossRef](#)]
26. Yang, C.G.; Jiang, Y.M.; Na, J.; Li, Z.J.; Cheng, L.; Su, C.Y. Finite-time convergence adaptive fuzzy control for dual-arm robot with unknown kinematics and dynamics. *IEEE Trans. Fuzzy Syst.* **2019**, *27*, 574–588. [[CrossRef](#)]

27. Makarov, M.; Grossard, M.; Rodriguez-Ayerbe, P.; Dumur, D. Modeling and preview H_∞ control design for motion control of elastic-joint robots with uncertainties. *IEEE Trans. Ind. Electron.* **2016**, *63*, 6429–6438. [[CrossRef](#)]
28. Liu, X.G.; Liao, X.F. Fixed-time H_∞ control for port-controlled hamiltonian systems. *IEEE Trans. Autom. Control* **2019**, *64*, 2753–2765. [[CrossRef](#)]
29. Ortega, R.; Schaft, A.; Maschke, B.; Escobar, G. Interconnection and damping assignment passivity-based control of port-controlled Hamiltonian systems. *Automatica* **2022**, *38*, 585–596. [[CrossRef](#)]
30. Ortega, R.; Garcia-Canseco, E. Interconnection and damping assignment passivity-based control: A survey. *Eur. J. Control* **2004**, *10*, 432–450. [[CrossRef](#)]
31. Zhang, M.; Borja, P.; Ortega, R.; Liu, Z.T.; Su, H.Y. PID passivity-based control of port-hamiltonian systems. *IEEE Trans. Autom. Control* **2018**, *63*, 1032–1044. [[CrossRef](#)]
32. Zhai, J.Y.; Li, Z.Y. Fast-exponential sliding mode control of robotic manipulator with super-twisting method. *IEEE Trans. Circuits Syst.-II Express Briefs* **2022**, *69*, 489–493. [[CrossRef](#)]
33. Freidovich, L.; Robertsson, A.; Shiriaev, A.; Johansson, R. LuGre-model-based friction compensation. *IEEE Trans. Control Syst. Technol.* **2010**, *18*, 194–200. [[CrossRef](#)]
34. Azizi, Y.; Yazdizadeh, A. Passivity-based adaptive control of a 2-DOF serial robot manipulator with temperature dependent joint frictions. *Int. J. Adapt. Control Signal Process.* **2019**, *33*, 512–526. [[CrossRef](#)]
35. Yu, H.S.; Yu, J.P.; Liu, J.; Song, Q. Nonlinear control of induction motors based on state error PCH and energy-shaping principle. *Nonlinear Dyn.* **2013**, *72*, 49–59. [[CrossRef](#)]
36. Meng, X.X.; Yu, H.S.; Zhang, J.; Yang, Q. Adaptive EPCH strategy for nonlinear systems with parameters uncertainty and disturbances. *Nonlinear Dyn.* **2023**, *111*, 7511–7524. [[CrossRef](#)]
37. Meng, X.X.; Yu, H.S.; Zhang, J.; Yan, K.J. Optimized control strategy based on EPCH and DBMP algorithms for quadruple-tank liquid level system. *J. Process. Control* **2022**, *110*, 121–132. [[CrossRef](#)]
38. Meng, X.X.; Yu, H.S.; Zhang, J. An EPCH control strategy for complex nonlinear systems with actuator saturation and disturbances. *Inf. Sci.* **2023**, *625*, 639–655. [[CrossRef](#)]

Disclaimer/Publisher’s Note: The statements, opinions and data contained in all publications are solely those of the individual author(s) and contributor(s) and not of MDPI and/or the editor(s). MDPI and/or the editor(s) disclaim responsibility for any injury to people or property resulting from any ideas, methods, instructions or products referred to in the content.